Research on Active Flow Control Method of NACA0012 Airfoil with Traveling Wave Structure

Q. Dai[1], E. Qi[1], S. Huang[1], Z. Zhou[1] and Y. Wang[1, 2†]

[1.]*Shanghai key laboratory of multiphase flow and heat transfer of power engineering, School of Energy and Power Engineering, University of Shanghai for Science and Technology, Shanghai 200093, China*
[2.]*National Key Laboratory of Science and Technology on Aerodynamic Design and Research, Xi'an, 710072, China*

†Corresponding Author Email: wangying@usst.edu.cn

ABSTRACT

Traveling wave is an innovative active flow control technique that can remarkably mitigate flow separation. This paper employs numerical simulation to examine how traveling wave structures affect the NACA0012 airfoil. The traveling wave structure is situated at $0.5\%c$ from the leading edge. In the chord direction, its projection length is $0.1c$. Through numerical simulation, the impacts of dimensionless length-width ratio and velocity of traveling wave on flow separation are investigated, and the relationship between the traveling wave's optimal parameters and angle of attack is explored. The outcomes demonstrate that traveling waves with suitable length-width ratios and velocities can effectively suppress flow separation. When $AoA=16°$, traveling wave airfoil with dimensionless velocity $U=1.1$ and length-width ratio $A=1$ achieves the best performance, and its lift-drag ratio is 9.24 times that of the original NACA0012 airfoil. The optimal dimensionless length-width ratio and velocity of the traveling wave airfoil are associated with the angle of attack, and different parameters need to be chosen at various angles of attack to attain optimum effect.

1. INTRODUCTION

Airfoils, serving as the fundamental elements of wind turbine blades, significantly impact both flow characteristics and aerodynamic performance, thereby playing a crucial role in enhancing energy efficiency. However, airfoils tend to stall as angle of attack is high, causing flow separation, which reduces its aerodynamic performance and flow characteristics. Therefore, flow control on wind turbine blades aims at restraining flow separation, delaying stall, and improving lift-drag ratio.

To promote the aerodynamic performance, researchers have proposed numerous methods for airfoil flow control (Khalil et al., 2020). Flow control is a technique that improves the mechanical performance of fluid by altering the motion state of the fluid, besides it is classified into passive and active flow control (Kral, 2000). Passive flow control refers to a flow control method that works without external energy (Genç et al., 2020). For example, Wang et al. (2019b) explored the dynamic characteristics of the combined control of downward hinge flap and downward deflected spoiler. This paper examined the lift-drag ratio, stall angle, and other parameters under different flap and spoiler deflection angles, and concluded that the combined control of

downward hinged flap and downward deflected spoiler can competently delay stall and improve the lift-drag ratio. Wang et al. (2017) scrutinized how vortex generators with different parameters affect the dynamic characteristics of S809 airfoil through numerical simulation methods, such as lift, drag, flow separation, and other dynamic characteristics. This exploration indicated that vortex generators are effective passive flow control devices that can improve the boundary layer performance, thus increasing the power coefficient, and reducing load fluctuation and noise of wind turbines. Ni et al. (2019) designed a downward-inclined slot on the NACA 63_4-021 airfoil. They analyzed the aerodynamic performance under various slot parameters by experiment and numerical simulation, concluded that slot design can substantially improve blade aerodynamic performance. They also discovered that a 14% enhancement in the airfoil's maximum lift-drag ratio was possible. Wang et al. (2019a) added fixed winglets on the S809 airfoil, which effectively suppressed flow separation and delayed stall angle. In comparison to the reference airfoil, the lift coefficient enhanced by 52.99%. They also found that adding a passive control structure at the appropriate position boosted the aerodynamic performance remarkably, when the flow separation does not occur, it may increase the drag or reduce the structural strength of airfoils.

NOMENCLATURE			
A	dimensionless length-width ratio	t	time
A_w	maximum length-width ratio of the traveling wave	U	dimensionless velocity
C_d	drag coefficient	U_w	velocity of the traveling wave
C_{d1}, C_{d2}, C_{d3}	drag coefficient of different grid numbers	U_∞	incoming flow velocity
C_l	lift coefficient	W	wave width
C_{l1}, C_{l2}, C_{l3}	lift coefficient of different grid numbers	u_i, u_j	time-averaged flow velocity components
C_l/C_d	lift-drag ratio	u_i', u_j'	fluctuating flow velocity components
c	chord length	λ_w	projection length of the traveling wave
L	wave length	ρ	density
p	time-averaged pressure	v	kinematic viscosity

Active flow control refers to a flow control method that requires external energy (Aubrun et al., 2017). For example, Shan et al. (2008) investigated the impacts of nanosecond dielectric barrier discharge plasma actuator (NS-DBDPA) on NACA0012 airfoil's aerodynamic force and flow field at various Reynolds numbers through numerical simulation and wind tunnel experiments. They also revealed that NS-DBDPA could enhance the momentum inside the boundary layer by generating periodic or non-periodic disturbances, resist the adverse pressure gradient, delay or suppress flow separation. Similarly, Vorobiev et al. (2013) researched the lift enhancement influence of plasma flow controller on NACA0009 airfoil at low Reynolds number through experiments. They demonstrated that the plasma flow controller was an effective flow control technology, with the advantages of no mechanical parts, quick response, low power consumption, and low noise. Mazaheri et al. (2016) applied plasma excitation on DU 91-W2-250 airfoil, and showed that a plasma controller could increase the C_l and C_l/C_d by 160% and 180%, respectively, and delay stall. Gilarranz et al. (2005) employed a novel synthetic jet actuator (SJA) on NACA0015 airfoil, and discovered the lift coefficient of airfoils promoted by 80%. Zhao et al. (2017) established a motion-embedded mesh technique, which was utilized in airfoil baseline dynamic stall simulation. By comparing experimental and simulation outcomes to verify the effectiveness. The research exhibited that the synthetic jet might enhance the airfoil's aerodynamic performance and rotor's dynamic stall characteristics. Moreover, Atik et al. (2005) used the boundary layer upper method to suppress dynamic stall, and indicated that boundary layer upper started at an early stage, and even a weak upper could inhibit flow separation effectively. Petz and Nitsche (2007) added a blowing device on the trailing edge flap. Through experimental research, they observed that the flow separation was controlled effectively, as well as the lift-drag ratio was promoted by 20% approximately. Generally, the active control methods can improve the flow characteristics and the aerodynamic performance significantly. In recent years, Reinforcement Learning has been proven to be a great tool for defining the movement of flow control systems. For example, Vinuesa et al. (2022) employed new flow control methods for enhancing wing aerodynamic efficiency using Deep Reinforcement Learning (DRL), and demonstrated that DRL could develop novel control approaches in sophisticated turbulence. Similarly, Rabault et al. (2019) achieved active flow control of airfoils with Artificial Neural Networks (ANN) trained by DRL. In a two-dimensional simulation (*Re*=100), they reported that the ANN stabilized the vortex streets and decreased drag by about 8%. Portal-Porras et al. (2023) controlled the movement of a rotating flap on the NACA0012 airfoil with RL, and improved its aerodynamic performance.

Traveling wave deformation is an active flow control method that generates traveling waves along the airfoil direction by applying periodic deformation on the airfoil surface. This method can increase the fluid velocity in the direction of flow, or inject energy into the fluid at the airfoil's leading edge. Di et al. (2017) fitted NACA0012 airfoils with vibrating membranes which were on the upper surface, it varied the vibration amplitude and frequency to suppress flow separation. They reported that the vibrating membrane could elevate the lift coefficient, reduce the drag coefficient, and improve flow fields. However, at the airfoil leading edge, this control method uses the periodic vibration of the flexible membrane, which does not increase the energy in the fluid flow direction. Hence, investigating a flow control method that injects energy into the flow direction, conducted at the airfoil's leading edge, holds remarkable significance for improving aerodynamic characteristics.

A traveling wave vibration device is attached to the NACA0012 airfoil at $0.5\%c$ from the leading edge. Firstly, the reliability of numerical simulation is verified. Secondly, the effects of different traveling wave velocities and length-width ratios on the airfoils are studied. Finally, the correlation between the optimal traveling wave parameters and angle of attack is examined.

2. CALCULATION MODEL AND METHOD

2.1 Geometric Model

Luo et al. (2011) arranged the synthetic jet at $0.01c$ from the leading edge. They proposed that placing the control points should be where the flow separation started. Therefore, this paper refers to the research of Luo et al. (2011) and adopts the same installation position for a traveling wave structure. The traveling wave structure is situated at $0.5\%c$ from the leading edge, and its projection
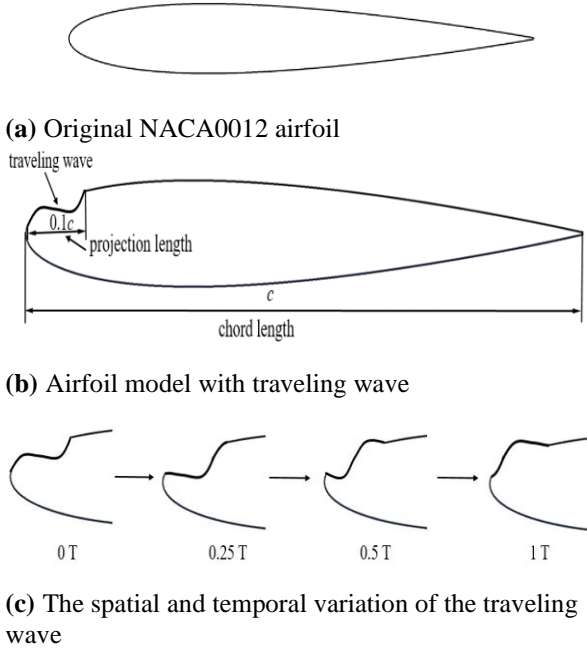
(a) Original NACA0012 airfoil

(b) Airfoil model with traveling wave

0 T   0.25 T   0.5 T   1 T

(c) The spatial and temporal variation of the traveling wave

Fig. 1 Geometric model

length is $0.1c$. The projection length refers to the straight distance between the starting and ending points after projecting the traveling wave onto the chord. The original NACA0012 airfoil and traveling wave airfoil model are shown in Fig. 1.

The motion equation of a traveling wave structure can be represented as Eq. (1):

$$y_w(x_w, t) = y_w(x_w, t-1) - A_w \cdot (x_w - 0.005) \cdot (0.105 - x_w) \cdot cos\left[\frac{2\pi}{\lambda_w}(x_w - U_w t_w) + \varphi\right] \quad (1)$$

where $y_w(x_w,t)$, $y_w(x_w,t-1)$ are the y coordinates of a certain moment and the previous moment, x_w is the x coordinate of a certain moment, λ_w, A_w, U_w represent the projection length, maximum length-width ratio and velocity of traveling waves.

Taking the incoming flow velocity (U_∞) and chord length (c) as characteristic velocity and scale, the above equation are dimensionless as follows:

$$x = \frac{x_w}{c}, y = \frac{y_w}{c}, A = \frac{A_w}{c}, \lambda = \frac{\lambda_w}{c}, \ U = \frac{cU_w}{U_\infty}, \ t = \frac{U_\infty t_w}{c}$$

Therefore, the dimensionless motion equation of the traveling wave can be described as Eq. (2):

$$y(x, t) = y(x, t-1) - A \cdot (x - 0.005) \cdot (0.105 - x) \cdot cos\left[\frac{2\pi}{\lambda}(x - Ut) + \varphi\right] \quad (2)$$

2.2 Physical Model and Calculation Setup

The aerodynamic characteristics are numerically simulated with $Re=1.2\times10^5$, $Ma=0.0052$. The flow field is unsteady because of large angles of attack, while the fluid is incompressible due to the low incoming Mach number. Therefore, the incompressible Navier-Stokes (RANS) equation is used as the governing Eqs. (1) and (2).

$$\frac{\partial u_i}{\partial x_i} = 0 \quad (3)$$

$$\frac{\partial u_i}{\partial t} + u_j\frac{\partial u_i}{\partial x_j} = \frac{1}{\rho}\frac{\partial p}{\partial x_i}$$
$$+ \frac{\partial}{\partial x_j}\left[v\left(\frac{\partial u_i}{\partial x_j} + \frac{\partial u_j}{\partial x_i}\right)\right] \quad (4)$$
$$- \overline{u_i' u_j'}$$

where t represent the time, x_i represent the space Cartesian coordinates, u_i, u_j represent the components of time-averaged flow velocity and u_i', u_j' represent the components of fluctuating flow velocity. v, p, and ρ represent the kinematic viscosity, and time-averaged pressure, density, respectively.

A hybrid grid scheme is employed to discretize the two-dimensional computational domain for higher accuracy. Unstructured grids are used in the traveling wave part, while O-shaped structured grids are employed for the remaining domain. The overall grid plot and grid division close to the airfoil are displayed in Fig. 2. When $c=1$ m, $Re=1.2\times10^5$, then $U_\infty=1.75288$ m/s. Finally, to guarantee $y^+ < 1$, the first layer has a mesh height of 3.14×10^{-4} m. The calculation domain size is set as 50 times the chord length. In ANSYS Fluent, the *SST k-ω* model Menter (1993) was selected as the turbulence model, relying on the exploration of Di et al. (2017) and Liu et al. (2019). This model is a widely used eddy viscosity model in the numerical simulation field of wind turbine airfoils (Liu et al., 2019; Kim & Kim 2020; Bhavsar et al., 2023; Ye et al., 2023). Meanwhile, the second-order accuracy was selected for the solution, and the first-order upwind scheme was applied to turbulence constants, as shown in Table 1.

Table 1 Numerical simulation settings for airfoils

Numerical solution methods	Details
Simulation software	Ansys Fluent
Turbulence model	*SST k-ω* turbulence model
Scheme of pressure-velocity coupling	Simple solver
Turbulent Kinetic Energy	First order upwind
Specific Dissipation Rate	First order upwind
Boundary condition	
Inlet	Velocity boundary condition
	Turbulent intensity=0.1%
	Turbulent viscosity ratio=10
Outlet	Pressure boundary condition
	Gauge pressure (Pascal)=0
	Turbulent intensity=0.1%
	Turbulent viscosity ratio=10
wall	no-slip

X=0.005 m

pressure outlet

velocity inlet

X=0.025 m
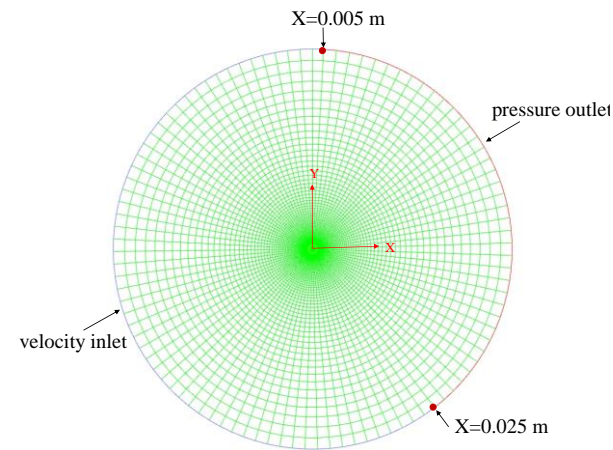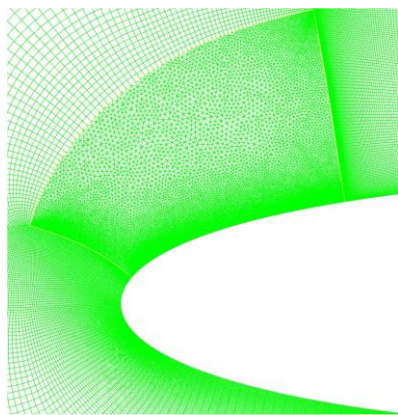
(a) Overall grid plot

(b) Grid near the leading edge of the airfoil
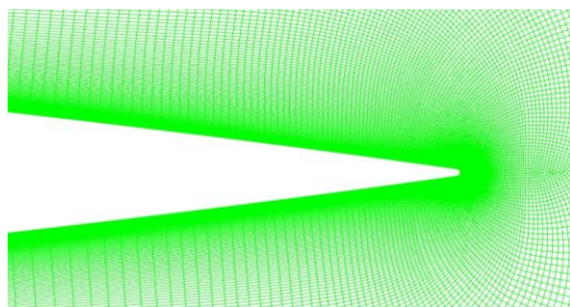
(c) Grid near the trailing edge of the airfoil

Fig. 2 The overall grid plot and grid division near the airfoil

Table 2 Numbers and names of three sets of grids

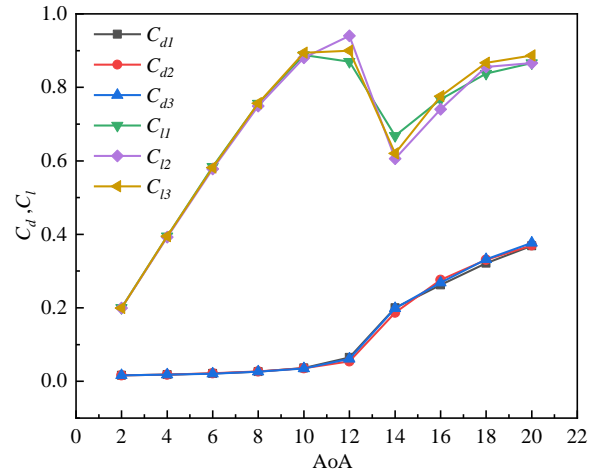| Name	Number
Mesh-1	49247
Mesh-2	102765
Mesh-3	209581

Fig. 3 Grid independence verification
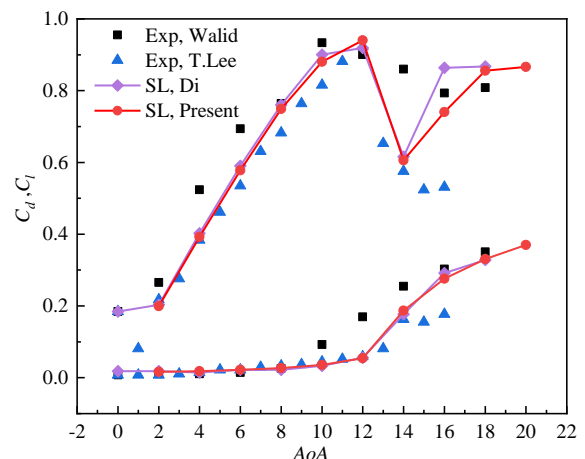
Fig. 4 Comparison of the lift and drag coefficient of airfoils with angle of attack

2.3 Numerical Simulation Verification

For the grid of a two-dimensional airfoil, to prove the grid independence, three cases of grids with diverse numbers are obtained by altering the nodes number on the airfoil wall under the condition that other settings remain unchanged. The specific grid numbers and names of the three sets of grids are exhibited in Table 2. From Fig. 3, three sets of grids are employed to calculate the flow around the NACA0012 airfoil at the angle of attack (AoA) from 2° ~20°. C_d, C_l represent the drag and lift coefficient of the airfoil, C_{l1}, C_{l2} and C_{l3} correspond to the lift coefficient for diverse grid numbers, C_{d1}, C_{d2} and C_{d3} correspond to the drag coefficient for diverse grid numbers. From Fig. 3, at small angles of attack (when $AoA \leqslant 10°$), C_l and C_d calculated by the three sets of grids are almost the same, indicating that there is no obvious

flow separation at this condition. When $AoA > 10°$, the C_l and C_d calculated by the three sets of grids begin to differ, indicating that complex phenomena such as separation and shock waves occur in the flow. When $AoA = 12°$, C_l and C_d of Mesh-1 are smaller, C_d of Mesh-2 and Mesh-3 are closer. When $AoA = 14°$, there is a small difference between C_l and C_d with three cases of grids. When AoA is large, due to the complex flow structure and deep stall, it is difficult to simulate accurately, and this small difference caused by the number of grids is acceptable. Therefore, considering both the calculation accuracy and efficiency, Mesh-2 is selected for further calculation.

Figure 4 compares the numerical simulation results with the experiment data from Chakroun et al. (2004) and
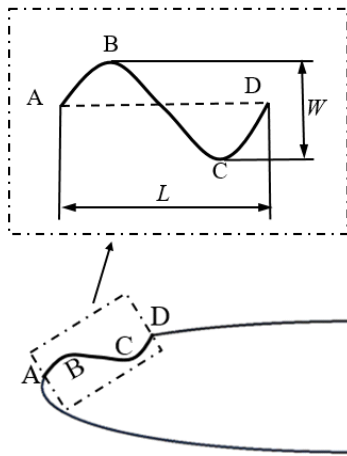
**Fig. 5 Schematic diagram of the length-width ratio of the traveling wave**

Lee and Gerontakos (2004), as well as numerical simulation results from Di et al. (2017). From Fig. 4, the C_l and C_d obtained by the numerical simulation are close to the experimental results of Chakroun et al. (2004) and Lee and Gerontakos (2004) when *AoA* is below 10°. However, when *AoA* is above 12°, the numerical simulation results diverge from the experimental results, although the overall trends of C_l and C_d are consistent. This is because the airfoil undergoes a rigid stall near *AoA*=12°, where the flow structure and aerodynamic characteristics become complex. Figure 4 also shows a large experiment dissimilarity in C_l and C_d from Chakroun et al. (2004) and Lee and Gerontakos (2004) when *AoA* is above 12°, which may be caused by experimental errors or uncertainties. However, the numerical simulation results agree well with those of Di et al. (2017), which suggests that the numerical simulation can predict the aerodynamic performance of actual airfoils accurately.

3. COMPUTATIONAL RESULTS AND ANALYSIS

The length-width ratio and traveling wave velocity are important parameters that affect the traveling wave airfoil performance. The length-width ratio is defined as the ratio of wavelength L to wave width W, wavelength is the straight distance from point A to point D, and wave width is the perpendicular distance from point B to point C, as shown in Fig. 5. The numerical simulation is employed to investigate the impact of dimensionless length-width ratio (A) and velocity (U) on C_l, C_d, and flow field structure of NACA0012 airfoil when *AoA*=16°. The relationship between stall angle and aerodynamic performance is also investigated.

3.1 Effects of Dimensionless Length-Width Ratio on Traveling Wave Airfoil

The dimensionless length-width ratio has a significant influence on the traveling wave airfoil, the C_l and C_d exhibit periodic fluctuations with time. Fig. 6 and Fig. 7 show the variation of the C_l and C_d of airfoils with different length-width ratios when U=1. The analysis is based on the stable fluctuations of C_l and C_d, which occur 2 seconds after the periodicity of the curves is established.
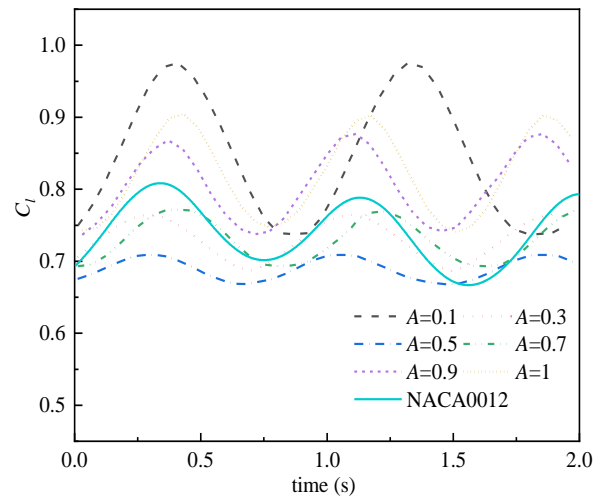
(a) Variation of the lift coefficient
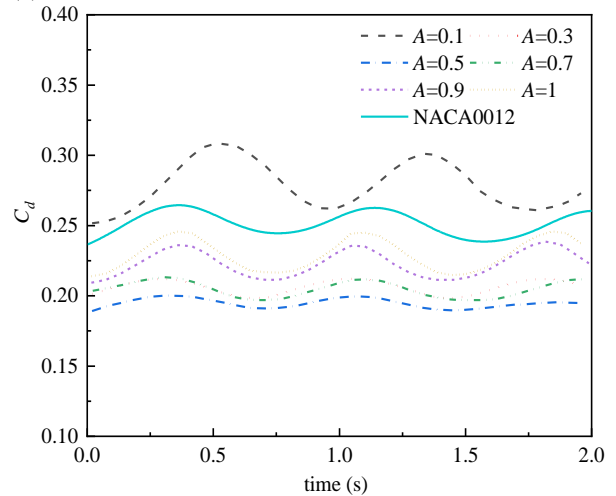
(b) Variation of the drag coefficient

Fig. 6 Variation of the lift and drag coefficient (different length-width ratios when *AoA*=16°)

From Fig. 6(a), the traveling wave airfoil with the length-width ratio of 0.9 or 1 has a higher lift coefficient (C_l) than the original NACA0012 airfoil, while the traveling wave airfoil with the length-width ratio of 0.1 has a lower and more fluctuating lift coefficient (C_l), indicating that the lift is unstable and affected by external factors. When the length-width ratio is 0.3, 0.5, and 0.7, the fluctuation of C_l with time gradually decreases, and the values of peak and valley are lower, although C_l is more stable at this time, the traveling wave airfoil has a lower lift coefficient. From Fig. 6(b), the traveling wave airfoil with a length-width ratio of 0.1 has a higher drag coefficient than the original NACA0012 airfoil, while traveling wave airfoils with other length-width ratios have lower drag coefficients than the original NACA0012 airfoil. Compared to the original NACA0012 airfoil, traveling wave airfoils with length-width ratios of 0.9 or 1 possess higher lift coefficients and lower drag coefficients. Besides, Fig. 7 exhibits that the C_l/C_d is increased by 19.01% and 17.7%, respectively. Therefore, the traveling wave vibration airfoil with an appropriate length-width ratio has an obvious effect on improving the lift coefficient and enhancing the aerodynamic performance effectively.
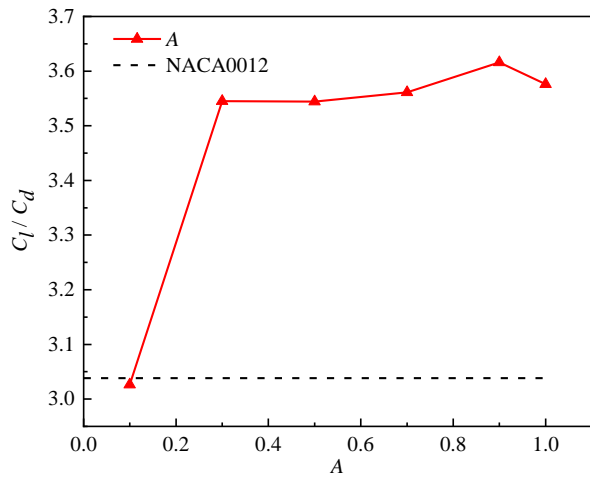
Fig. 7 Variation of the lift-drag ratio (different length-width ratios when *AoA*=16°)

(a) *A*=0.1   (b) *A*=0.3

(c) *A*=0.5   (d) *A*=0.7

(e) *A*=0.9   (f) *A*=1

Z Vorticity -20 -18 -16 -14 -12 -10 -8 -6 -4 -2 0 2 4 6 8 10 12 14 16 18 20

Fig. 9 Streamline and vorticity nephogram near traveling wave airfoils (different length-width ratios when *AoA*=16°)

Z Vorticity -20 -18 -16 -14 -12 -10 -8 -6 -4 -2 0 2 4 6 8 10 12 14 16 18 20
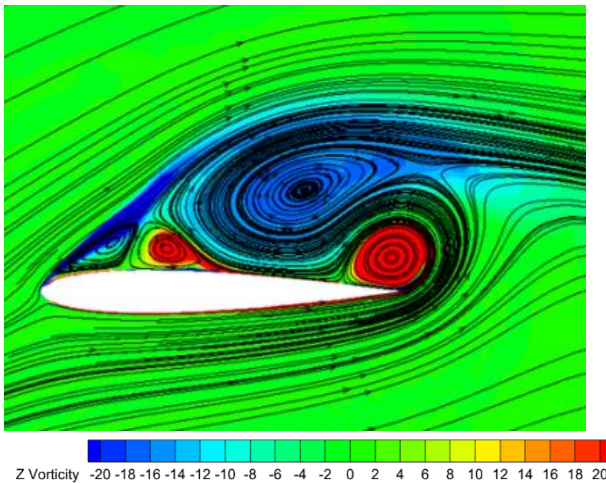
Fig. 8 Streamline and vorticity nephogram near the original NACA0012 airfoil

Figure 8 displays the instantaneous streamline and vorticity nephogram near NACA0012 airfoil when *AoA*=16°. From Fig. 8, a separation vortex covers the upper surface of the airfoil, flow separation occurs near the leading edge because there exists a negative vortex. The negative vortex refers to the vortex region with a clockwise direction. The counterclockwise rotating flow separation zones are generated between the negative vortex zone and the airfoil to balance the clockwise vorticity area of the negative vortex zone.

Figure 9 shows the instantaneous streamline and vorticity nephogram near the traveling wave control airfoil with different length-width ratios when *AoA*=16°. The traveling wave airfoil has a smaller vortex structure area than the original NACA0012 airfoil, and the negative vortex shrinks in size. Moreover, the negative vortex area decreases as the dimensionless length-width ratio *A* increases. The lift-drag ratio improves effectively as *A* is greater than or equal to 0.3. This is because the traveling wave control airfoil delays the flow separation, which suppresses the large-scale separation vortex on the upper surface. As well as C_d reduces significantly, which is
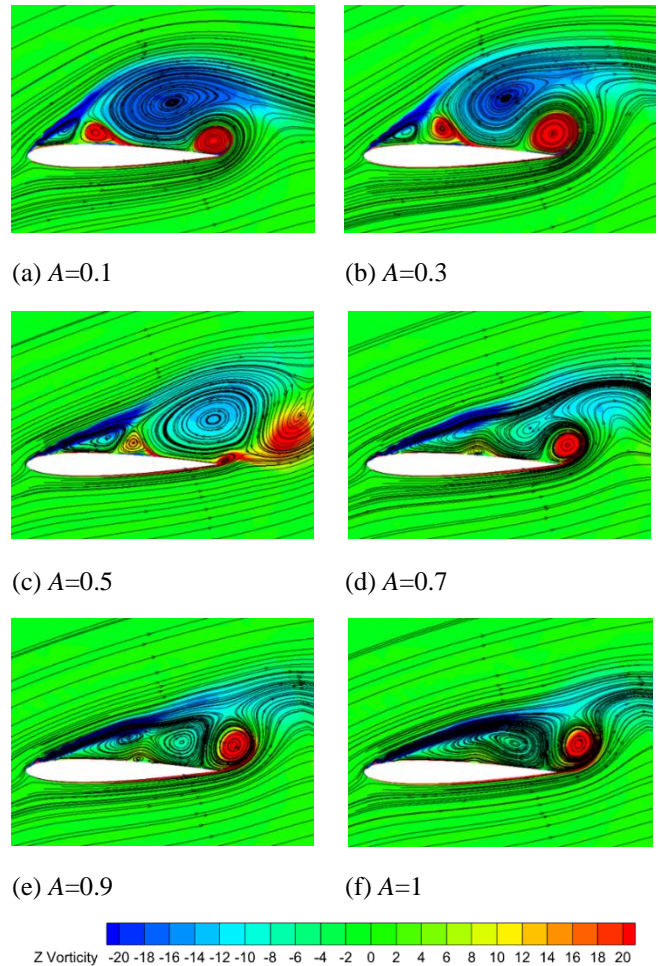
consistent with the conclusion in Fig. 7 that C_l/C_d improves effectively.

3.2 Effects of Dimensionless Velocity on Traveling Wave Airfoil

Traveling wave velocity is also an important parameter that affects the aerodynamic characteristics and flow field. The influence of different traveling wave velocities on the C_l and C_d exhibit periodic fluctuations with time. Fig. 10 and Fig. 11 show the variation of the C_l and C_d under different traveling wave velocities, respectively.

Figure 10 and Fig. 11 show the change of the C_l and C_d of airfoils with different traveling wave velocities when the length-width ratio *A*=1, respectively. From Fig. 10, C_l of the traveling wave airfoil is higher than NACA0012 airfoil when the dimensionless velocity *U* is between 0.8 and 1.2. The lift coefficient reduces as the traveling wave velocity increases when *U* is between 0.9 and 1.05, but increases significantly and fluctuates greatly when *U*=1.1. In Fig. 11, the traveling wave airfoils have higher drag coefficients than the original NACA0012 airfoil when *U*=0.8 or 1.2, while the lift coefficient does not increase much when *U*=1.15. However, when *U*=1.1, the lift coefficient significantly increases, showing significant
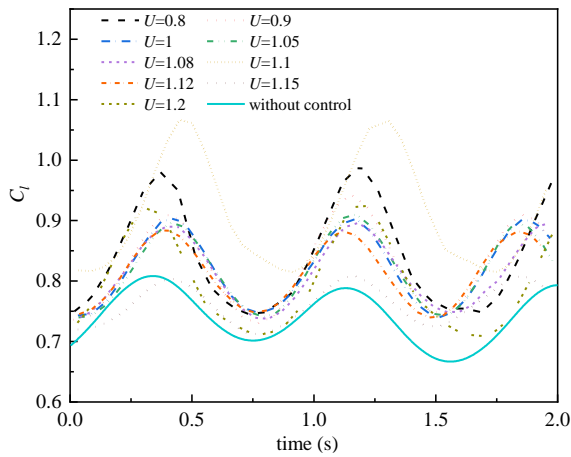
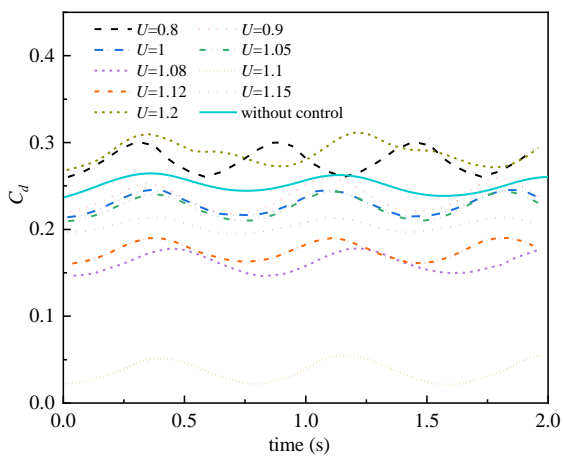**Fig. 10 Variation of the lift coefficient (different traveling wave velocities)**

Fig. 12 Variation of the lift-drag ratio (different traveling wave velocities)

Fig. 11 Variation of the drag coefficient (different traveling wave velocities)

fluctuations over time. The maximum C_l and minimum C_l are 31.91% and 16.38% higher than the original NACA0012 airfoil, respectively. This suggests that the optimal aerodynamic performance of traveling wave airfoils is achieved as the dimensionless velocity U near 1.1. From Fig. 11, the drag coefficient varies with the traveling wave velocity. When U is between 0.9 and 1.05, the drag coefficient decreases while the traveling wave velocity increases; when U=1.1, the drag coefficient shows the most significant reduction, and its maximum and minimum values are 78.84% and 90.86% lower than the original NACA0012 airfoil. Figure 12 compares the variation of the C_l/C_d between the traveling wave airfoils with different velocities and the original NACA0012 airfoil. The traveling wave airfoil has a lower lift-drag ratio when U=0.8 or 1.2, but higher lift-drag ratio when U=1.1. This is consistent with Fig. 10 and Fig. 11, which show that when U=1.1, the C_l increases, while the C_d decreases. Therefore, the aerodynamic performance is improved only when the traveling wave dimensionless velocity during an appropriate range (U=0.9~1.15). Within the dimensionless velocity range studied, U=1.1 is the optimal traveling wave velocity, and the lift-drag ratio improves significantly, which positively affects the aerodynamic performance.
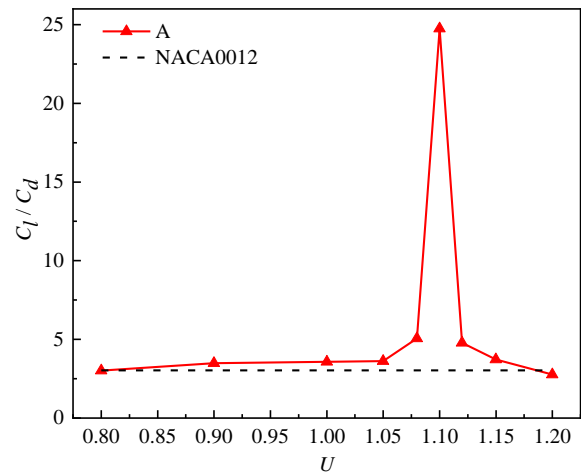
Figure 13 exhibits the instantaneous streamline near airfoils with different traveling wave velocities (U). The traveling wave velocity affects the vortex structure and the aerodynamic characteristic. Relative to the flow field of NACA0012 airfoil, when U=0.8 or 1.2, the large-scale clockwise separated vortex on the upper surface is smaller, while the anticlockwise separated vortex on the trailing edge is smaller and closer to the wall. As a result, the C_l/C_d is lower than the original NACA0012 airfoil. When U=1.15 or in the range of 0.9 ~ 1.05, a smaller-scale vortex structure forms near the traveling wave, and compared to the original airfoil, it has a greater distance from the leading edge. This can remarkably increase the lift coefficient, mitigate flow separation, and decrease the drag coefficient. When U=1.1, compared with NACA0012 airfoil flow field, the large-scale clockwise separation vortex is smaller, and the counterclockwise separation vortex formed at the tail is farther from the trailing edge, the traveling wave can reduce the flow disturbance near the airfoil effectively. Moreover, when U=1.1, the traveling wave speed is slightly higher than the speed of incoming flow, supplying enough kinetic energy to the airfoil. Therefore, the sufficient kinetic energy and the reduced flow disturbance account for the substantial enhancement in the lift-drag ratio.

Figure 14 indicates the surface pressure variation of traveling wave airfoils at different velocities. The figure reveals that the traveling wave airfoil has lower surface pressure than the original NACA0012 airfoil. According to Bernoulli's theorem, the higher the flow velocity, the lower the pressure, which implies that the airfoil increases its lift. The traveling wave vibration causes irregular fluctuations of the surface pressure near the traveling wave structure, while the rest of the airfoil surface has a similar pressure distribution to the original NACA0012 airfoil. When U=1.15 or in the range of 0.9 ~ 1.05, the traveling wave airfoil has a much lower pressure on the upper surface near the trailing edge, however, between the lower and upper surfaces exists a larger pressure difference. When the traveling wave velocity increases, the pressure on trailing edge decreases and the C_l/C_d increases. When U=1.2, the surface pressure near the trailing edge's upper
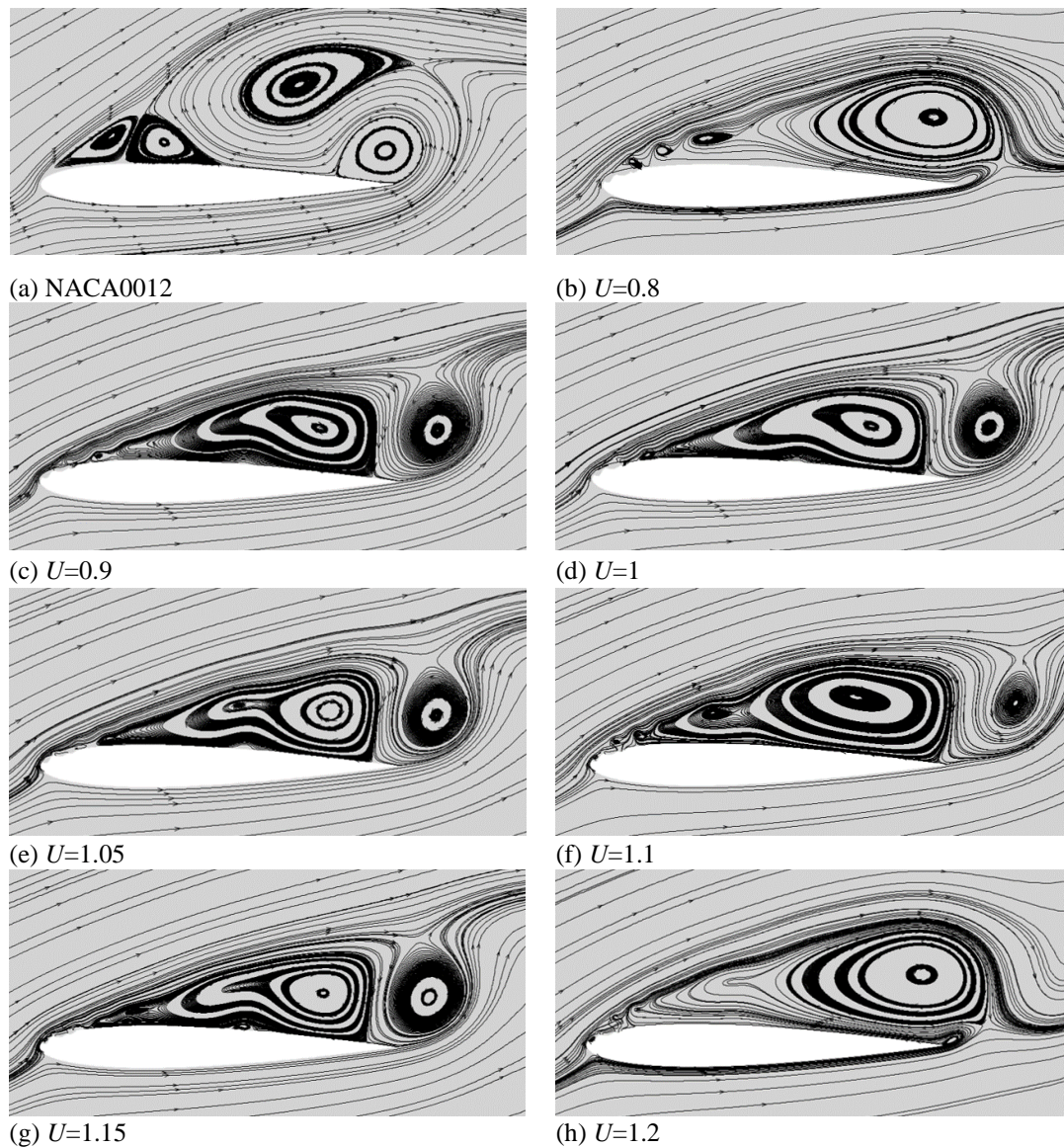
(a) NACA0012

(b) U=0.8

(c) U=0.9

(d) U=1

(e) U=1.05

(f) U=1.1

(g) U=1.15

(h) U=1.2

Fig. 13 Instantaneous streamline near airfoils with different traveling wave velocities

Fig. 14 Surface pressure variation of traveling wave airfoils with different velocities

is illustrated by Fig. 12. When U=1.1, the surface pressure is the lowest on the upper surface near trailing edge, and the pressure difference is larger. This causes a higher lift coefficient, a lower drag coefficient, and a better aerodynamic performance. It is consistent with Fig. 13, which shows that the traveling wave vibration enhances the flow separation.

Figure 15 displays the velocity nephogram near the airfoil with different traveling wave velocities under the same traveling wave length-width ratio. From Fig. 15, when U=1.1, the fluid velocity near the trailing edge increases significantly. This indicates that the dynamic pressure of trailing edge increases, a larger pressure difference between the lower and upper surfaces. Meanwhile, the wake area becomes smaller, the drag coefficient decreases. From the above, the traveling wave velocity within a reasonable range will strengthen the momentum exchange near the airfoil and increase the vortex intensity. This leads to a higher lift coefficient, a lower drag coefficient, and better aerodynamic characteristics.
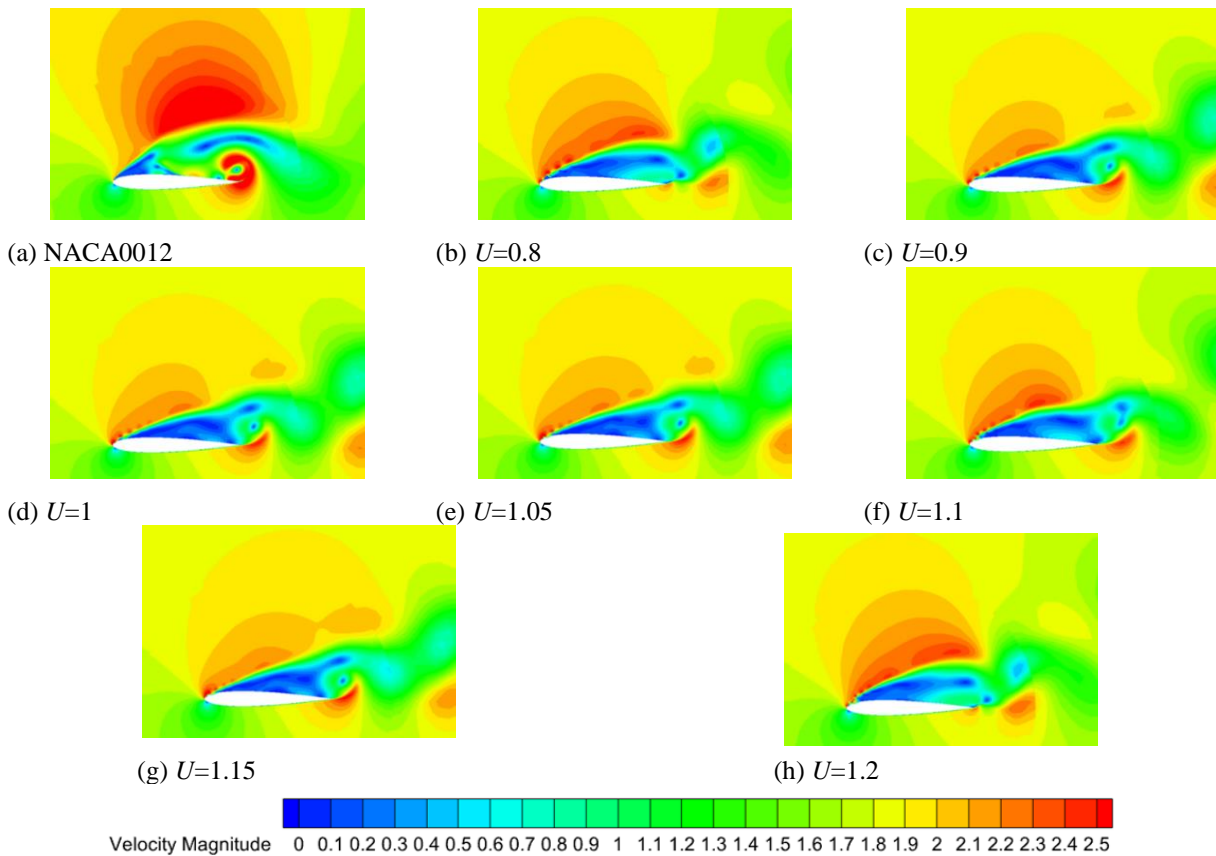
surface first increases and then decreases, there is a small pressure difference between the lower and upper surfaces. This causes the C_d increases while the C_l/C_d decreases, as

(a) NACA0012   (b) *U*=0.8   (c) *U*=0.9

(d) *U*=1   (e) *U*=1.05   (f) *U*=1.1

(g) *U*=1.15   (h) *U*=1.2

Velocity Magnitude 0 0.1 0.2 0.3 0.4 0.5 0.6 0.7 0.8 0.9 1 1.1 1.2 1.3 1.4 1.5 1.6 1.7 1.8 1.9 2 2.1 2.2 2.3 2.4 2.5

Fig. 15 Velocity nephogram near airfoils with different traveling wave velocities

3.3 Simulation Results of Traveling Wave Airfoils with Different Angles of Attack

The traveling wave airfoil belongs to active flow control method, and the optimal traveling wave parameters and control effect of this method, under different stall angles of attack, are mainly evaluated by improving the aerodynamic performance and optimizing flow field. The lift-drag ratio is an important index to reflect the aerodynamic performance of airfoils. As mentioned above, the C_l/C_d is the largest when $AoA=16°$, $U=1.1$ and $A=1$, it is 9.24 times that of the original NACA0012 airfoil, and is considered as the optimal traveling wave velocity and length-width ratio within studied range. Di et al. (2017) proposed that the optimal dimensionless frequency and amplitude of the vibrating diaphragm are related to the stall angle of attack. To prove that the traveling wave structure has similar properties, at other angles of attack, the traveling wave airfoil with $U=1.1$ and $A=1$ has a poorer aerodynamic performance than $AoA=16°$. Therefore, the aerodynamic characteristic and flow field structure of the traveling wave airfoil were studied under various angles of attack when $U=1.1$ and $A=1$.

Figure 16 exhibits the variation of C_l and C_d at various angles of attack. From Fig. 16, compared with the original NACA0012 airfoil, the traveling wave airfoil with dimensionless velocity $U=1.1$ and the length-width ratio $A=1$, has smaller lift coefficient and larger drag coefficient when AoA is small. When $AoA=14°$, the lift-drag ratio increased by 19.13%. When $AoA>14°$, the traveling wave airfoil has higher lift coefficient and lower drag
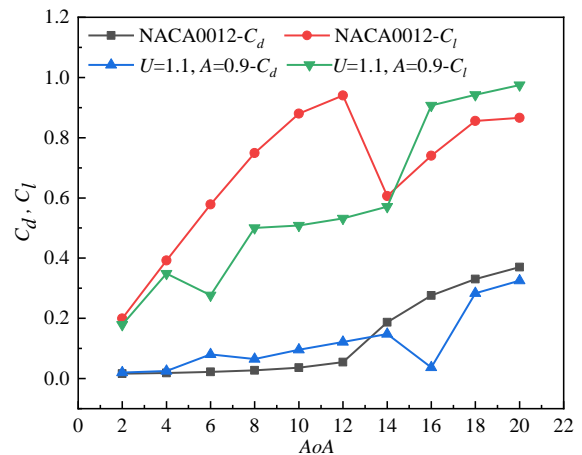

Fig. 16 Variation of the lift and drag coefficient at various angles of attack

coefficient. Therefore, when AoA is high, the traveling wave airfoil with $U=1.1$ and $A=1$ can significantly improve the aerodynamic performance.

Figure 17 and Fig. 18 show the velocity nephogram near the traveling wave airfoil ($U=1.1$, and $A=1$) and the original NACA0012 airfoil when AoA between 2° and 20°. From Fig. 17, when AoA increases, a slender low-speed region appears on the upper surface near the leading edge. When AoA continues to increase, the low-speed region around the airfoil breaks, the momentum exchange of the fluid near the airfoil becomes more intense, indicating flow separation. The fluid velocity near the trailing edge also increases. From Fig. 18, there is an obvious low-speed
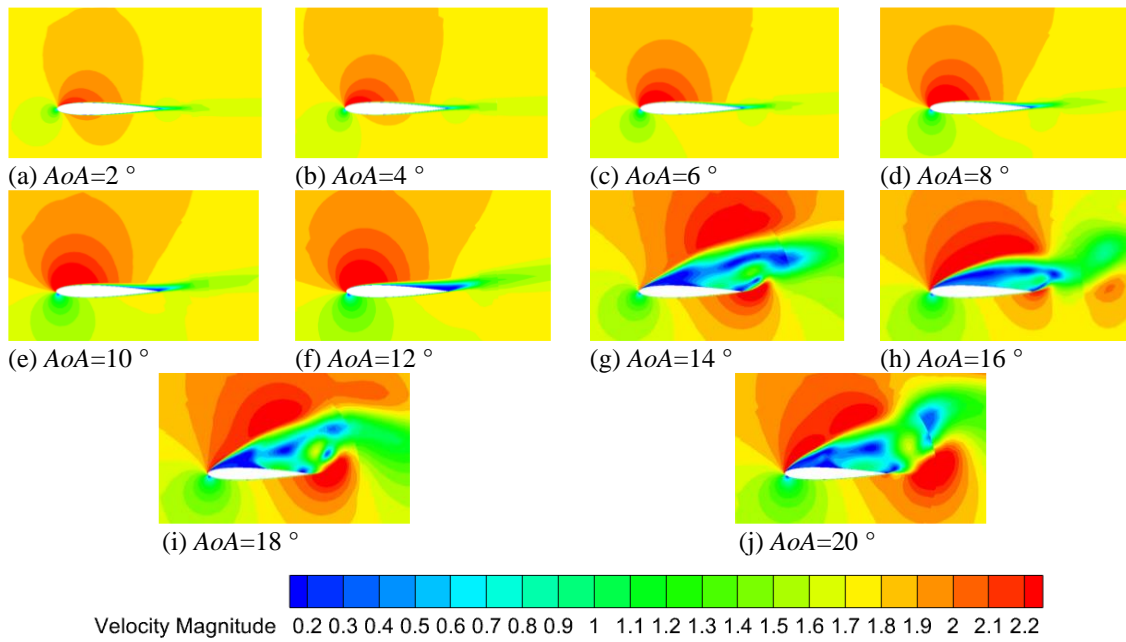
(a) *AoA*=2 °   (b) *AoA*=4 °   (c) *AoA*=6 °   (d) *AoA*=8 °

(e) *AoA*=10 °   (f) *AoA*=12 °   (g) *AoA*=14 °   (h) *AoA*=16 °

(i) *AoA*=18 °   (j) *AoA*=20 °

Velocity Magnitude 0.2 0.3 0.4 0.5 0.6 0.7 0.8 0.9 1 1.1 1.2 1.3 1.4 1.5 1.6 1.7 1.8 1.9 2 2.1 2.2

Fig. 17 Velocity nephogram of NACA0012 airfoil at various angles of attack

(a) *AoA*=2 °   (b) *AoA*=4 °   (c) *AoA*=6 °   (d) *AoA*=8 °

(e) *AoA*=10 °   (f) *AoA*=12 °   (g) *AoA*=14 °   (h) *AoA*=16 °

(i) *AoA*=18 °   (j) *AoA*=20 °

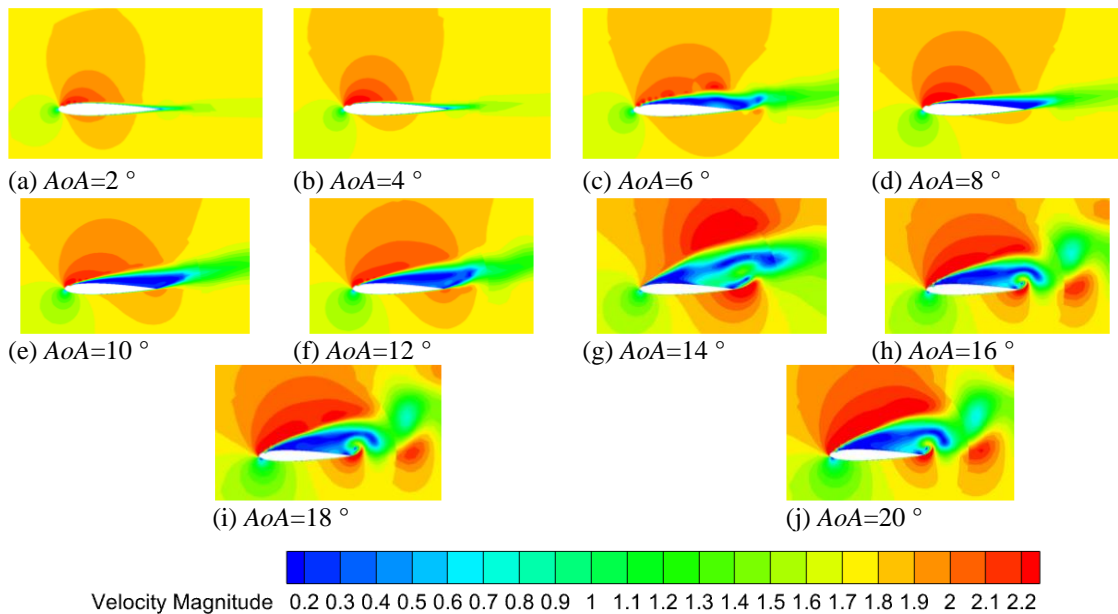Velocity Magnitude 0.2 0.3 0.4 0.5 0.6 0.7 0.8 0.9 1 1.1 1.2 1.3 1.4 1.5 1.6 1.7 1.8 1.9 2 2.1 2.2

Fig. 18 Velocity nephogram of the traveling wave airfoil with *U*=1.1 and *A*=1 at various angles of attack

region near the airfoil when *AoA*=6°. This is because when *AoA* is small, the motion of the traveling wave accelerates the momentum exchange between surrounding fluids and induces flow separation. The flow separation region is significantly smaller than other stall angles of attack when *AoA*=16°. At this time, due to the impacts of the traveling wave structure, the flow separation is effectively controlled. This illustrates that the impacts of traveling wave structure on aerodynamic performance are connected with angle of attack.

Figure 19 and Fig. 20 show the vorticity contour and streamline near the original NACA0012 airfoil and the traveling wave airfoil with *U*=1.1, and *A*=1 When *AoA* between 2° and 20°. Figure 19 shows that the original NACA0012 airfoil generates vortex structures when

AoA=12°. The flow separation region and drag increase with the angle of attack. From Fig. 20, the traveling wave airfoil generates vortex structures when *AoA*=6°. Due to the motion of traveling waves, the flow separation region does not increase linearly with the angle of attack. Compared with the NACA0012 airfoil, when *AoA* is large, the traveling wave airfoil has a smaller flow separation region and a greater distance from the leading edge, which indicates that the traveling wave can enhance the aerodynamic performance. Fig. 20 also exhibits that the vortex structure is the smallest, the lift-drag ratio is promoted most significantly when *AoA*=16°. This suggests that the combination of *U*=1.1 and *A*=1 is the optimal dimensionless velocity and length-width ratio when
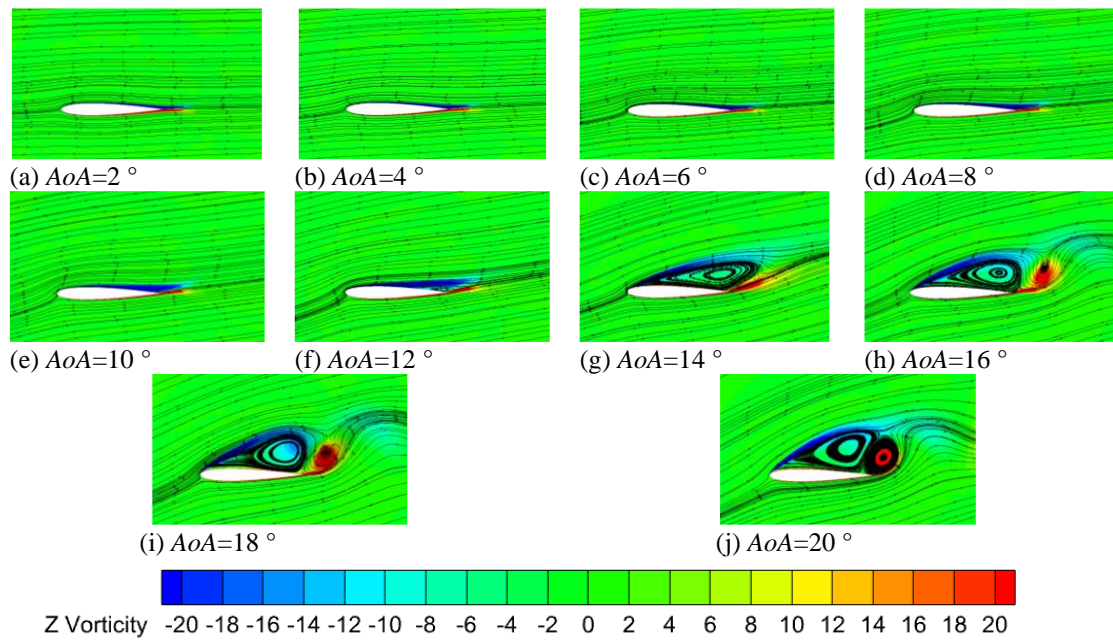
(a) *AoA*=2 ° (b) *AoA*=4 ° (c) *AoA*=6 ° (d) *AoA*=8 °

(e) *AoA*=10 ° (f) *AoA*=12 ° (g) *AoA*=14 ° (h) *AoA*=16 °

(i) *AoA*=18 ° (j) *AoA*=20 °

Z Vorticity -20 -18 -16 -14 -12 -10 -8 -6 -4 -2 0 2 4 6 8 10 12 14 16 18 20

Fig. 19 Vorticity nephogram and streamline of NACA0012 airfoil at various angles of attack

(a) *AoA*=2 ° (b) *AoA*=4 ° (c) *AoA*=6 ° (d) *AoA*=8 °

(e) *AoA*=10° (f) *AoA*=12 ° (g) *AoA*=14 ° (h) *AoA*=16 °

(i) *AoA*=18 ° (j) *AoA*=20 °

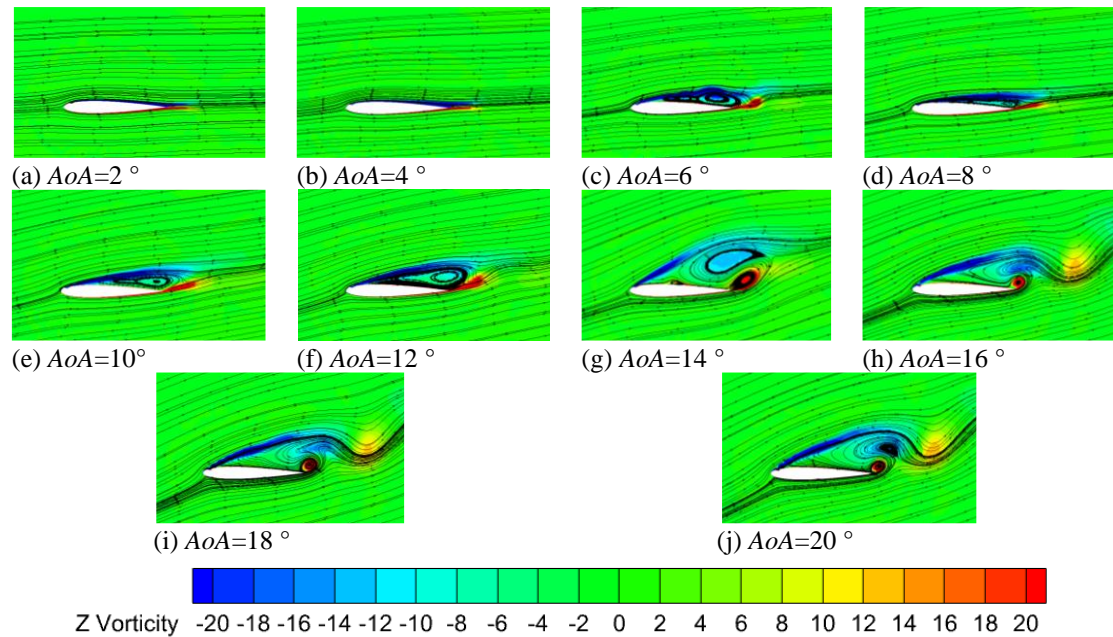Z Vorticity -20 -18 -16 -14 -12 -10 -8 -6 -4 -2 0 2 4 6 8 10 12 14 16 18 20

Fig. 20 Vorticity nephogram and streamline of traveling wave airfoil with U=1.1 and A=1 at various angles of attack

AoA=16°. In summary, the optimal dimensionless parameters (such as *U* and *A*) of the traveling wave airfoil are related to the angle of attack. Various optimal values should be chosen for different angles of attack to suppress flow separation and improve the lift-drag ratio.

4. CONCLUSION

This article investigates the NACA0012 airfoil and introduces a flow control method that injects energy along the flow direction at the leading edge of airfoils. The traveling wave structure is located at $0.5\%c$ from the leading edge, and its projection length is $0.1c$. By changing the velocity and length-width ratio of the traveling wave to suppress flow separation, numerical simulation was employed to study the effects of different traveling wave velocities and length-width ratios on lift, drag, and flow separation of the airfoil. The optimal parameters of the traveling wave airfoil for different angles of attack were also determined and discussed.

(1) With the length-width ratio of 0.9 or 1, the traveling wave control airfoil has a 19.01% and 17.7% higher lift-drag ratio than the original NACA0012 airfoil, respectively. An optimal length-width ratio for the traveling wave vibration airfoil is able to enhance the aerodynamic performance through delaying flow separation, reducing the negative vortex area, increasing the lift-drag ratio.

(2) The dimensionless velocity (*U*) of the traveling

wave is instrumental in ameliorating the aerodynamic performance. When U is between 0.9 and 1.15, the lift coefficient and lift-drag ratio increase, while the drag coefficient decreases. When U=1.1, the lift-drag ratio has significant improvement, and the airfoil almost obtains the best aerodynamic performance. Meanwhile, the flow separation area is the smallest, the negative vortex region is the smallest, and the pressure drop trend on the trailing edge's upper surface is obvious.

(3) The traveling wave injects energy into the fluid flow along the leading edge, altering the distribution of flow fields by changing the velocity and shape of the leading edge. Traveling wave structures can reduce surface pressure and shrink the vortex area at high angles of attack. The traveling wave within a reasonable velocity range can delay the separation of flow at the leading edge, weaken the separation vortex at the trailing edge, and enhance the aerodynamic performance.

(4) When the angle of attack is high, the traveling wave structure can enhance aerodynamic performance and suppress flow separation by injecting energy into the fluid flow. However, the optimal dimensionless velocity U and length-width ratio A of the traveling wave airfoil are related to angle of attack, and various parameters are required for various angles of attack to optimize the effect. This paper shows that the traveling wave airfoil with U=1.1 and A=1 achieves the best performance when AoA=16°, with a lift-drag ratio 9.24 times higher than the original NACA0012 airfoil. When AoA is below 14°, the traveling wave airfoil has a worse aerodynamic performance because the motion of the traveling wave promotes flow separation. Therefore, the optimal traveling wave parameters for various angles of attack are the focus of further research.

ACKNOWLEDGEMENTS

CONFLICT OF INTEREST

The authors have no conflicts to disclose.

AUTHORS CONTRIBUTION

Qingwen Dai: Investigation, Writing - Original Draft; **Ershuai Qi**: Methodology, Investigation; **Shengxian Huang**: Investigation; **Zikang Zhou**: Revision; **Ying Wang**: Conceptualization; Writing - Review & Editing; Supervision.

REFERENCES

Atik, H., Kim, C. Y., Van Dommelen, L. L., & Walker, J. D. A. (2005). Boundary-layer separation control on a thin airfoil using local suction. *Journal of Fluid Mechanics*, *535*, 415-443. https://doi.org/10.1017/S002211200500501X

Aubrun, S., Leroy, A., & Devinant, P. (2017). A review of wind turbine-oriented active flow control strategies. *Experiments in Fluids*, *58*, 1-21. 10.1007/s00348-017-2412-0

Bhavsar, H., Roy, S., & Niyas, H. (2023). Aerodynamic performance enhancement of the DU99W405 airfoil for horizontal axis wind turbines using slotted airfoil configuration. *Energy*, *263*, 125666. https://doi.org/10.1016/j.energy.2022.125666

Chakroun, W., Al-Mesri, I., & Al-Fahad, S. (2004). Effect of surface roughness on the aerodynamic characteristics of a symmetrical airfoil. *Wind Engineering*, *28*(5), 547-564. https://doi.org/10.1260/0309524043028136

Di, G., Wu, Z., & Huang, D. (2017). The research on active flow control method with vibration diaphragm on a NACA0012 airfoil at different stalled angles of attack. *Aerospace Science and Technology*, *69*, 76-86. https://doi.org/10.1016/j.ast.2017.06.020

Genç, M. S., Koca, K., Demir, H., & Açıkel, H. H. (2020). Traditional and new types of passive flow control techniques to pave the way for high maneuverability and low structural weight for UAVs and MAVs. *Autonomous Vehicles*, 131-160. 10.5772/intechopen.90552

Gilarranz, J. L., Traub, L. W., & Rediniotis, O. K. (2005). A new class of synthetic jet actuators-part II: application to flow separation control. *Journal of Fluids Engineering*, *127*(2), 377-387. https://doi.org/10.1115/1.1882393

Khalil, Y., Tenghiri, L., Abdi, F., & Bentamy, A. (2020). Improvement of aerodynamic performance of a small wind turbine. *Wind Engineering*, *44*(1), 21-32. https://doi.org/10.1177/0309524X19849847

Kim, S. H., & Kim, K. Y. (2020). Effects of installation location of fluidic oscillators on aerodynamic performance of an airfoil. *Aerospace Science and Technology*, *99*, 105735. https://doi.org/10.1016/j.ast.2020.105735

Kral, L. D. (2000). Active flow control technology. *ASME Fluids Engineering Technical Brief*, 1-28.

Lee, T., & Gerontakos, P. (2004). Investigation of flow over an oscillating airfoil. *Journal of Fluid Mechanics*, *512*, 313-341. https://doi.org/10.1017/S0022112004009851

Liu, Q., Miao, W., Li, C., Hao, W., Zhu, H., & Deng, Y. (2019). Effects of trailing-edge movable flap on aerodynamic performance and noise characteristics of VAWT. *Energy*, *189*, 116271. https://doi.org/10.1016/j.energy.2019.116271

Luo, D. H., Sun, X. J., Huang, D. G., & Wu, G. Q. (2011). Flow control effectiveness of synthetic jet on a stalled airfoil. *Proceedings of the Institution of Mechanical Engineers, Part C: Journal of Mechanical Engineering Science*, 225(9), 2106-2114. https://doi.org/10.1177/0954406211407255

Mazaheri, K., Omidi, J., & Kiani, K. C. (2016). Simulation

of DBD plasma actuator effect on aerodynamic performance improvement using a modified phenomenological model. *Computers & Fluids*, *140*, 371-384. https://doi.org/10.1016/j.compfluid.2016.10.015

Menter, F. R. (1993). *Zonal two equation k-ω turbulence models for aerodynamic flows.* 24th Fluid Dynamics Conference. Orlando, Florida. 10.2514/6.1993-2906

Ni, Z., Dhanak, M., & Su, T. C. (2019). Improved performance of a slotted blade using a novel slot design. *Journal of Wind Engineering and Industrial Aerodynamics*, *189*, 34-44. 10.1016/j.jweia.2019.03.018

Petz, R., & Nitsche, W. (2007). Active separation control on the flap of a two-dimensional generic high-lift configuration. *Journal of Aircraft*, *44*(3), 865-874. https://doi.org/10.2514/1.25425

Portal-Porras, K., Fernandez-Gamiz, U., Zulueta, E., Garcia-Fernandez, R., & Berrizbeitia, S. E. (2023). Active flow control on airfoils by reinforcement learning. *Ocean Engineering, 287*, 115775. https://doi.org/10.1016/j.oceaneng.2023.115775

Rabault, J., Kuchta, M., Jensen, A., Réglade, U., & Cerardi, N. (2019). Artificial neural networks trained through deep reinforcement learning discover control strategies for active flow control. *Journal of fluid mechanics, 865,* 281-302. https://doi.org/10.1017/jfm.2019.62

Shan, H., Jiang, L., Liu, C., Love, M., & Maines, B. (2008). Numerical study of passive and active flow separation control over a NACA0012 airfoil. *Computers & Fluids*, *37*(8), 975-992. https://doi.org/10.1016/j.compfluid.2007.10.010

Vinuesa, R., Lehmkuhl, O., Lozano-Durán, A., & Rabault, J. (2022). Flow control in wings and discovery of novel approaches via deep reinforcement learning. *Fluids*, *7*(2), 62. https://doi.org/10.3390/fluids7020062

Vorobiev, A., Rennie, R. M., & Jumper, E. J. (2013). Lift enhancement by plasma actuators at low Reynolds numbers. *Journal of Aircraft*, *50*(1), 12-19. https://doi.org/10.2514/1.C031249

Wang, H., Jiang, X., Chao, Y., Li, Q., Li, M., Zheng, W., & Chen, T. (2019a). Effects of leading edge slat on flow separation and aerodynamic performance of wind turbine. *Energy*, *182*, 988-998. 10.1016/j.energy.2019.06.096

Wang, H., Zhang, B., Qiu, Q., & Xu, X. (2017). Flow control on the NREL S809 wind turbine airfoil using vortex generators. *Energy*, *118*, 1210-1221. 10.1016/j.energy.2016.11.003

Wang, W., Breard, C., & Sun, Y. (2019b). *Numerical study of the high-lift aerodynamic characteristics of dropped hinge flap coupled with drooped spoiler.* The Proceedings of the 2018 Asia-Pacific International Symposium on Aerospace Technology (APISAT 2018) 9th (pp. 211-226). Springer Singapore. https://doi.org/10.1007/978-981-13-3305-717

Ye, X., Hu, J., Zheng, N., & Li, C. (2023). Numerical study on aerodynamic performance and noise of wind turbine airfoils with serrated gurney flap. *Energy*, *262*, 125574. https://doi.org/10.1016/j.energy.2022.125574

Zhao, Q., Ma, Y., & Zhao, G., (2017). Parametric analyses on dynamic stall control of rotor airfoil via synthetic jet. *Chinese Journal of Aeronautics*, *30*(6), 1818-1834. https://doi.org/10.1016/j.cja.2017.08.011